JOURNAL OF SYNCHROTRON RADIATION
ISSN 1600-5775

CT dosimetry at the Australian Synchrotron for 25–100 keV photons and 35–160 mm-diameter biological specimens

Stewart Midgley,[a]* Nanette Schleich,[b] Alex Merchant[c] and Andrew Stevenson[d,e]

[a]South Australian Medical Imaging, Australia, [b]Department of Radiation Therapy, University of Otago, Wellington, New Zealand, [c]Barwon Health, Victoria, Australia, [d]Australian Synchrotron, 800 Blackburn Road, Clayton, VIC 3168, Australia, and [e]CSIRO Future Industries, Private Bag 10, Clayton South, VIC 3169, Australia.
*Correspondence e-mail: stewart.midgley.phd@gmail.com

Received 24 July 2018
Accepted 20 December 2018

Edited by A. Momose, Tohoku University, Japan

Keywords: Australian Synchrotron Imaging and Medical Beamline; third harmonic; CT dosimetry; CT dose indices; CT dose length product; effective dose.

The dose length product (DLP) method for medical computed tomography (CT) dosimetry is applied on the Australian Synchrotron Imaging and Medical Beamline (IMBL). Beam quality is assessed from copper transmission measurements using image receptors, finding near 100% (20 keV), 3.3% (25 keV) and 0.5% (30–40 keV) relative contributions from third-harmonic radiation. The flat-panel-array medical image receptor is found to have a non-linear dose response curve. The amount of radiation delivered during an axial CT scan is measured as the dose in air alone, and inside cylindrical PMMA phantoms with diameters 35–160 mm for mono-energetic radiation 25–100 keV. The radiation output rate for the IMBL is comparable with that used for medical CT. Results are presented as the ratios of CT dose indices (CTDI) inside phantoms to in air with no phantom. Ratios are compared for the IMBL against medical CT where bow-tie filters shape the beam profile to reduce the absorbed dose to surface organs. CTDI ratios scale measurements in air to estimate the volumetric CTDI representing the average dose per unit length, and the dose length product representing the absorbed dose to the scanned volume. Medical CT dose calculators use the DLP, beam quality, axial collimation and helical pitch to estimate organ doses and the effective dose. The effective dose per unit DLP for medical CT is presented as a function of body region, beam energy and sample sizes from neonate to adult.

1. Introduction

Synchrotron light sources are combined with X-ray optics to enable computed tomography (CT) with near mono-energetic photon beams of selectable energy. Volume CT imaging using synchrotron radiation involves sample rotation about a vertical axis combined with vertical translation through a stationary horizontal beam that is 40–50 cm wide by 10–30 mm tall. The high degree of lateral spatial coherence of synchrotron sources enables X-ray analysis techniques that probe the complex refractive index (Wilkins *et al.*, 1996; Chapman *et al.*, 1997; Bravin *et al.*, 2013). Temporal coherence translates to near mono-energetic radiation that is employed to measure the X-ray linear attenuation coefficient μ, while the ability to select beam energy enables materials characterization via K-edge subtraction (KES) (Schlomka *et al.*, 2008) and dual-energy X-ray analysis (DEXA) (Jackson & Hawkes, 1981; Midgley & Schleich, 2015). Source brightness coupled with extended scan times can lead to substantial radiation absorbed dose to the sample.

This study investigates CT-specific dose metrics (Bushberg *et al.*, 2012; IMPACT, 1998) for the range of beam energies delivered by the monochromator at the Australian Synchro-

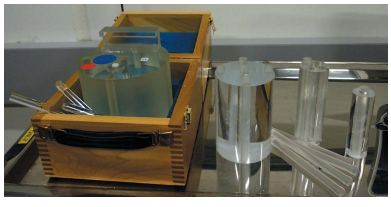

tron Imaging and Medical Beamline (IMBL). In both human and animal imaging, dosimetry estimates are the first step in minimizing the risk of radiation producing adverse impacts on their wellbeing (ARPANSA, 2005; NHMRC, 2013). This paper presents measurements of CT dose metrics for synchrotron CT at 25–100 keV.

The paper is organized as follows. Operation of the beamline is described with strategies to control beam energy and dose rate. Modern medical CT scanners are briefly reviewed in terms of data acquisition, reconstructed image quality and CT dosimetry via the dose length product (DLP) method. The beam quality and influence of harmonic radiations (Tran *et al.*, 2003) were investigated by measuring transmission through copper with an image receptor. Dose rate in air and absorbed dose to soft tissues were measured with ion chambers placed in air or inside poly(methyl methacrylate) (PMMA) phantoms, respectively. The range of phantom sizes spanned from small animals, such as mice, to larger specimens with dimensions comparable to the adult human head. The results are presented as coefficients that scale the absorbed dose in air recorded by the in-beam ion chamber and reported as dose area product (DAP) rate, to estimate CT dose metrics. The CT DLP is used to estimate absorbed dose to individual organs and the effective dose.

Table 1
Summary of storage ring and IMBL SCMPW source parameters used for the experiment (standard mode) compared with operation at 1.4 T for lower energy and flux.

Numerical values are from [*a*] Stevenson & Di Lillo (2017), Table 3 in vacuo filter set F4, [*b*] Stevenson (2017), Tables 1, 2 and 4, or are to be determined (TBD).

Storage ring energy		3 GeV
Storage ring current		200 mA
Filtration	Front end	0.6 mm diamond
	Hutch 1A	0.45 mm graphene, 21.2 mm graphite, 2.8 mm Cu
	Hutch 1B	Nothing
	Hutch 2A [*a*]	0.7 mm Be, 0.076 mm Al, 2.83 mm Cu plus 162 mm He, 0.6 m air
	Hutch 2B	Nothing
	Hutch 3B	2.0 mm Be, 0.038 mm Al, 43 mm He, 2–4 m air

Wiggler operation	Standard mode	Lowest field
Wiggler magnetic field	3.0 T	1.4 T
Critical energy [*b*]	18.0 keV	8.4 keV
K [*b*]	14.6	6.8
Total radiated power	16 kW	3.5 kW
Energy for maximum flux [*b*]	87 keV	TBD
Energy weighted mean [*b*]	94 keV	TBD
Air kerma rate [*b*] at hutch 1B 24 m from the source in the central 1.1 ×1.1 mm^2	730 Gy s^{-1}	6.9 Gy s^{-1}

2. Materials and methods

2.1. CT studies at the IMBL

The IMBL utilizes a superconducting multipole wiggler (SCMPW) insertion device at the storage ring to produce intense white beam radiation for radiotherapy in Hutches 1 and 2. Wiggler radiation (see, for example, Attwood, 2000) is characterized by the magnetic deflection parameter K, critical energy representing the second quartile or half power boundary (for photon counting detection), weighted mean energy (for energy integrating detection) and the integrated power proportional to K^2. Applications include research for microbeam radiotherapy (Crosbie *et al.*, 2013) at absorbed dose rates in air and soft tissues of the order of hundreds of Grays per second. To utilize the same beam for diagnostic imaging while protecting the sample and image receptor from radiation damage, the following strategies are employed.

Beam energy is controlled in Hutch 1A by wavelength λ selection using a dual crystal bent Laue monochromator (DCBLM) in non-dispersive arrangement. The relationship for angle θ between the incident beam and silicon crystal planes with separation d is given by the Bragg equation,

$$n\lambda = 2d\sin(\theta), \tag{1}$$

to select the principal beam energy ($n = 1$) plus higher-order harmonics. The DCBLM is based on Si(111) Bragg reflection so harmonics come from odd *hkl* (*i.e.* 111, 333 *etc.*) plus those where $h + k + l = 4n$, and the largest contribution is from ($n = 3$) third-harmonic radiation (Stevenson *et al.*, 2012). The intensity of the selected beam is approximated by a power law of the form $1/E^m$ plus attenuation for transmission through approximately 2.5 mm of silicon. The DCBLM reduces the dose rate by three to four orders of magnitude and filtration by silicon imposes a low-energy cut-off of approximately 15 keV. The low-divergence beam travels 120 m to Hutch 3B while expanding in width to 40–50 cm, accompanied by a two orders of magnitude reduction in dose rate.

The dose rate at the sample can be further reduced by inserting attenuators into the path of the beam in Hutch 1A (see, for example, Crosbie *et al.*, 2013; Stevenson *et al.*, 2012, 2017), but at the cost of increasing the relative flux of harmonic radiation. Reducing the wiggler field lowers the dose rate and softens the spectrum to decrease harmonic contamination.

Instead, the DCBLM offers the following coarse control of beam intensity. The Bragg peak delivers the maximum dose rate and is used for rapid CT studies with strongly attenuating samples. 'Rocking off' to the region outside the peak delivers stable operation with one to two orders of magnitude reduced intensity for CT studies at lower dose rates. Between these extremes, operation on the shoulder region of the Bragg peak is sensitive to small changes in DCBLM orientation, which are amplified to produce larger variations in intensity that are to be avoided during CT data acquisition runs. SCMPW spectra are presented by Stevenson & Di Lillo (2017; Fig. 2) for the IMBL operated at 3.2 T, 3.0 T and at 1.4 T for the Advanced Photon Source (this spectrum is similar to that for the IMBL), while key spectral and dosimetry parameters are summarized in Table 1. Parameter K is proportional to field strength where lower values shift the wiggler spectrum to lower energies and reduce the total radiated power. Note that the beam reaching Hutch 3B undergoes additional filtering by the DCBLM (approximately 2.5 mm silicon) and the materials shown in

Table 1 for Hutches 2A and 3B. The contribution from harmonic radiation decreases for higher selected beam energies where the wiggler spectrum intensity falls and there is increased energy separation between principal and harmonic radiation. A major goal for this research was to determine the low-energy limit where the beam is no longer considered to be mono-energetic.

After making changes to the primary attenuators, collimation and Bragg angle, a time delay of 10 min allowed the DCBLM and other beamline components to reach thermal equilibrium. The image receptors require corrections for their dark signal, which usually does not change significantly over time, and for non-uniformities in the flat field, which arise from the beam optics, changes in ring current (now less than 0.25% whilst operated in top-up mode) and variations in the production and collection of light by the detection systems. We collect dark and flat images before and after each part of the experiment and use these to monitor changes in the beam profile and detector response over time periods of minutes to hours.

CT studies at the IMBL [see Midgley & Schleich (2015) for a schematic diagram] utilize a variety of luminescent screen and optical detection systems (Hall *et al.*, 2013) with screen thicknesses 10–50 µm and pixel sizes 5–100 µm. Asynchronous data acquisition with rotation about a vertical axis collects 1800 views over 180°. Reconstruction uses a parallel beam reconstruction algorithm for axial slices based on filtered back projection utilizing dedicated computing facilities. Reconstructions can be as finely sampled as the raw projection data or re-binned to improve image quality. Section 2.4 describes operation of a dedicated ion chamber for monitoring the incident dose rate in air at the sample.

2.2. Medical CT and dosimetry via the dose length product method

Medical CT moves the source and detector around a horizontal axis and stationary sample. Four decades of innovation have delivered technological advances in the design of the X-ray source, beam conditioning devices, detection system, optimization of exposure conditions and data processing methods (see, for example, Webb, 1990; Mahesh, 2009). Scan times have been reduced from minutes per slice to sub-second volume scanning for whole organs such as the brain and heart. Image quality achieves noise-to-signal ratios of 1% for $1 \times 1 \times 5\ \mathrm{mm}^3$ voxels, with patient doses reduced in accordance with the 'as low as reasonably achievable' (ALARA) principle (see, for example, ICRP, 2007). Medical CT beam quality is characterized by the use of a tungsten anode, peak accelerating voltage, 80–140 kVp, and beam filtration (equivalent to approximately 10 mm aluminium) that preferentially removes photon energies below 30 keV. Medical spectral CT based on simultaneous dual energy scanning (Petersilka *et al.*, 2008) is an emerging field that uses either fast kVp switching (Li *et al.*, 2011), dual layer energy-sensitive detection (Carmi *et al.*, 2005) or a dual source and detector array (Flohr *et al.*, 2006).

CT dose indices (CTDI) (see, for example, Bushberg *et al.*, 2012; Flower, 2012) are standardized measures of radiation in mGy delivered during the course of a CT scan. The absorbed dose arising from the collimated primary beam and scattering in the irradiated volume is integrated along the 100 mm axial length of a pencil dosimeter. The CT dose index in air (CTDIair) is measured at the axis of rotation for an axial scan, typically for a standard axial collimation of 10 mm, and is a measure of machine output. For patient dosimetry, the absorbed dose is measured inside special test objects known as phantoms that act as a substitute for the sample of interest. The adult head and abdomen are represented by 14 cm-long PMMA cylinders with diameters of 16 cm and 32 cm, respectively. The phantoms [see Fig. 1(*a*)] have cavities to receive the dosimeter or solid PMMA plugs, allowing absorbed dose delivered by the CT scan to be measured at the centre CTDIc and near the periphery CTDIp whereby the centre of the probe is at 20 mm depth. Medical CT takes the average of four peripheral positions (3, 6, 9 and 12 o'clock) to account for attenuation by the patient support. Fig. 1(*b*) shows typical variation in the absorbed dose with depth. The weighted absorbed dose CTDIw in the phantom is estimated by combining the central and average of the peripheral measurements weighted according to their approximate cross-sectional area via the relation

$$\mathrm{CTDIw} = \frac{1}{3}\mathrm{CTDIc} + \frac{2}{3}\mathrm{CTDIp}, \qquad (2)$$

representing the average dose to an axial slice of thickness 10 mm.

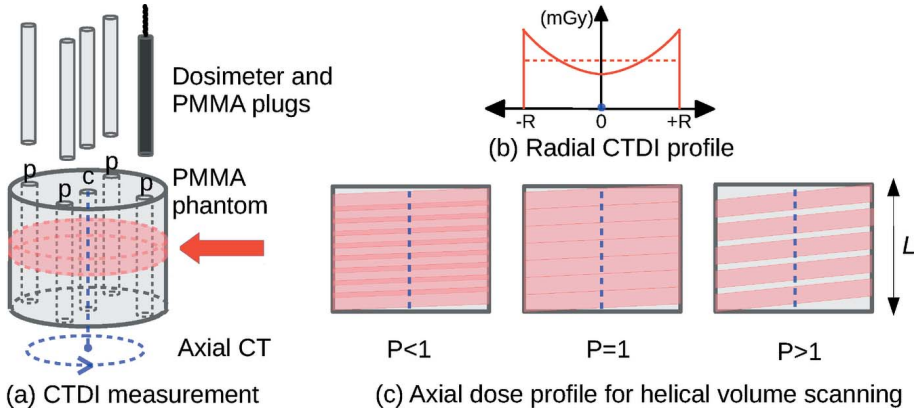

Figure 1
(*a*) CT dose indices are measured during axial CT scans of a soft tissue-like phantom with dosimeter placed at the centre c and periphery p. Typical radial and (dotted) average CTDI profiles (*b*), and schematic representation of axial dose profiles for helical volume scanning (*c*) along length L are shown.

Axial sampling during helical CT is illustrated in Fig. 1(*c*) and characterized by the helical pitch P representing the ratio of axial table feed per helical turn to axial beam collimation. Pitch is less than unity for overlapping helices, unity for helical CT and axial CT with no gaps, and greater than one when there are gaps between the helices. For helical CT scanning, the absorbed dose is inversely proportional to P and the volumetric CTDI is defined as

$$\mathrm{CTDIvol} = \frac{\mathrm{CTDIw}}{P}. \quad (3)$$

This relationship enables dosimetry measurements conducted in axial mode to be applied to CT scans of arbitrary pitch. For axial scan length L, the dose length product

$$\mathrm{DLP} = \mathrm{CTDIvol} \times L, \quad (4)$$

in mGy cm, is a measure of the absorbed dose to the scanned volume.

CT dose calculators such as IMPACT (IMPACT, 2011) and CTEXPO (Stamm & Nagel, 2002) use three-dimensional models for the body plus dose kernels obtained from Monte Carlo simulation for CT irradiation, in combination with the DLP, beam quality and details of the irradiation geometry (axial collimation, fan beam size and helical pitch) to estimate the absorbed dose to individual body organs.

The known thresholds for permanent deterministic effects in humans (ICRP, 2011, 2012) are 500 mGy to the eye (cataract induction), 500 mGy to the heart or brain (circulatory disease) and 6000 mGy to the skin (main erythema). Medical CT delivers organ doses that are usually below 50 mGy. Radiation weighting factors for photons and electrons are assumed to be unity (ICRP, 2007). Controversy exists though about the energy dependence of biological effects of photons and electrons, including, for example, studies showing evidence of increased relative biological effectiveness for electrons at energies below 5 keV (Nikjoo & Lindborg, 2010; Freneau *et al.*, 2018). Organ doses are combined with tissue weighting factors (Table 2) and summed over all tissues to estimate the effective dose in mSv. Fig. 2(*a*) presents the ratio of effective dose per unit DLP for medical CT of different scan regions, with beam qualities of 80–140 kVp, evaluated by Monte Carlo methods for the Oak Ridge National Laboratory (ORNL) whole-body phantom series (Cristy & Eckerman, 1987). The ratio is larger for regions containing more radiosensitive organs such as the abdomen, larger for weakly attenuating or smaller patients, and decreases for higher kVp as the beam is more penetrating. Fig. 2(*b*) presents the lifetime risk for all radiation-induced cancers (NRC, 2006). The lifetime risk of radiation-induced cancer incidence is approximately 0.05 Sv^{-1} for adults (20–40 years old), higher during childhood, higher for females, and decreases with age as fewer years are available in which to develop cancers. In light of these facts, medical CT uses lower DLP for children than adults for similar reconstructed image quality. Table 3 presents the current national diagnostic reference level (DRL) for adult medical CT, representing the third quartile for normal size patients, meaning 75% of patients receive lower DLP and effective dose.

Table 2
Tissue weighting factors W_T for humans (ICRP, 2007).

Organ	W_T	ΣW_T
Red bone-marrow, colon, lung, stomach, breast, remaining tissues†	0.12	0.72
Gonads	0.08	0.08
Bladder, oesophagus, liver, thyroid	0.04	0.16
Bone surface, brain, salivary glands, skin	0.01	0.04
Sum		1.00

† Remaining tissues: adrenals, extra-thoracic region, gall bladder, heart, kidneys, lymphatic nodes, muscle, oral mucosa, pancreas, prostate (male), small intestine, spleen, thymus, uterus/cervix (female).

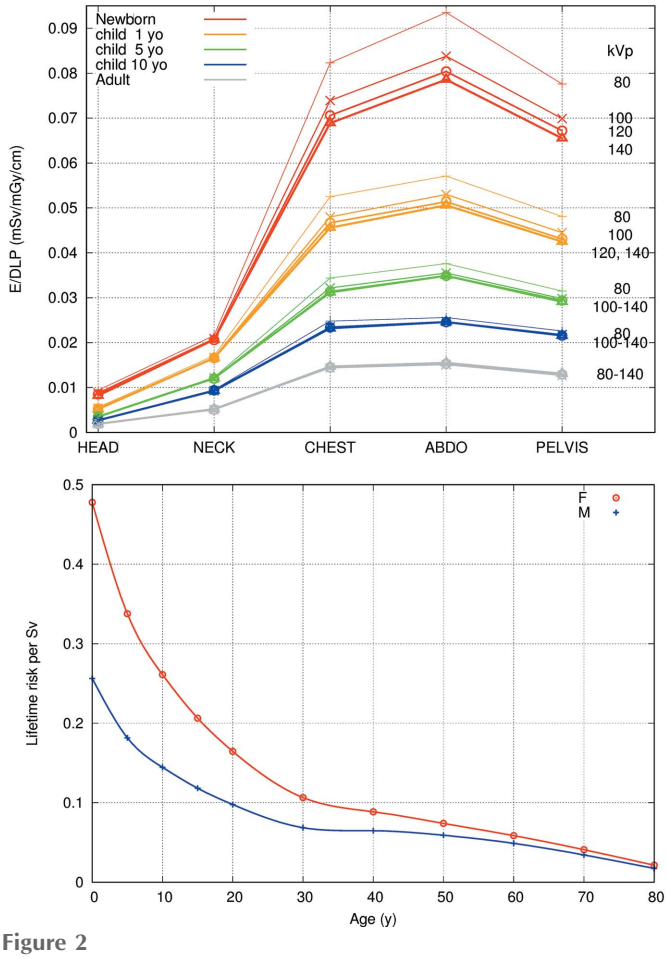

Figure 2
(*a*) Effective dose per unit DLP (Deak *et al.*, 2010) for CT scans of the ORNL whole-body phantom series using tungsten radiation at 80–140 kVp. (*b*) The lifetime risk for incidence of all radiation-induced cancers (NRC, 2006).

2.3. Beam quality measurements

Using the QUARTZ and RUBY imaging detectors (Hall *et al.*, 2013), the influence of third-harmonic radiation was investigated for beam energies 20–40 keV. Transmission measurements used 100 mm × 100 mm sized sheets of electrolytic grade copper of thicknesses 0.1–2.0 mm. The

Table 3
Medical CT third quartiles for CTDIvol (mGy) × scan length (cm) = DLP (mGy cm), for adult and paediatric CT (ARPANSA, 2011, 2012), with effective dose estimated for 120 kVp beam quality.

	Adult (15+ years)		Child (5–14 years)	
Protocol	DLP (mGy cm)	E (mSv)	DLP (mGy cm)	E (mSv)
Head	60 × 16.7 = 1000	1.9	35 × 17.1 = 600	1.6–2.1
Neck	30 × 20.0 = 600	3.1	–	–
Chest	15 × 30.0 = 450	6.5	5 × 22.0 = 110	2.6–3.5
Abdomen and pelvis	15 × 46.7 = 700	9.9	10 × 39.0 = 390	9.0–12.5
Chest, abdomen and pelvis	15 × 80.0 = 1200	17.0	–	–
Lumbar spine	40 × 22.5 = 900	11.6	–	–

QUARTZ image receptor (Hamamatsu model C9252DK-14) is a flat panel array (FPA) for dental radiography using an approximately 200 µm-thick CsI:Tl screen with 0.2 mm pixel size, a 243 mm × 123 mm field of view (FOV) and standard video frame rates of 30 frames s^{-1}. The RUBY image receptor (Monash University, Laboratory for Dynamic Imaging) uses an optical camera (PCO.edge CMOS with 2560 × 2160 pixels) that is optically coupled to a luminescent screen via a lens (Nikon Micro-Nikkor 105 mm/f 2.8 macro) and mirror system. The thickest available screen was utilized, a Gd_2O_2S:Tb phosphor screen from a Kodak Min-R mammography film cassette with 31.7 mg cm^{-2} or 43 µm thickness (Liaparinos *et al.*, 2006). The exponential attenuation law can be expressed as

$$\sum \mu t = -\ln(I_t/I_o), \tag{5}$$

where the left-hand side is known as the ray-sum. The maximum sample thickness for CT is controlled by statistical arguments (Rose & Shapiro, 1948; Nördfors, 1960; Midgley, 2006) and magnitude of the background or dark signal, and is at a maximum for ray-sums of about 5, or transmittance $T = I_t/I_o = 0.7\%$. For each of the principal energies investigated, suitable thicknesses of copper (Table 3) were arranged into a step wedge placed normal to the beam, with six steps spanning ray-sums of 0.5 to 5.0, which corresponds to total thicknesses ranging from 0.5 mm (30 keV) to 12 mm (100 keV).

The detection systems were operated just below their saturation values (8191 for QUARTZ and 65535 for RUBY), and the image noise was reduced during post-processing by averaging over many frames. Data acquisition collected 99 frames of background images with the beam shutter closed (representing detector dark signal) and 99 frames for exposure to the primary beam alone (representing detector flat images plus dark signal), and this process was repeated before and after recording 99 frames for transmission through the copper step wedge. The afterglow for CsI is 2% at 3 ms and 0.3% at 100 ms (van Eijk, 2002). This influence was avoided by excluding from analysis the first ten frames after opening or closing the beam shutter, to allow the signal to grow or decay to equilibrium values. The averages for the dark- and flat-field images were used for dark signal subtraction and for the flat-field correction, which compensates for spatial non-uniformities in the incident beam and the detector response. Analysis of the transmittance was performed by means of region-of-interest analysis using ImageJ (Schneider *et al.*, 2012). The mean and standard deviation were measured for regions covering the central third of each step, avoiding the lower and upper thirds where the vertical beam profile has reduced intensity leading to increased noise.

Results were expressed as the measured ray-sum calculated via equation (5) as a function of the expected or mono-energetic ray-sum, $\mu_0 t$, where μ_0 is the attenuation coefficient for zero thickness of absorber (defined below). The step wedge measurements were fitted to the following simple model,

$$\frac{I(t)}{I_o} = \frac{\exp(-\mu_1 t) + f\exp(-\mu_3 t)}{1+f}, \tag{6}$$

where t is the path length through copper, μ_1 and μ_3 are the attenuation coefficients for the principal and third harmonic, whose fractional contribution is $f/(1 + f)$. Note that f is weighted by the detection process, which includes factors for a three times increase in the amount of energy deposited and the reduced detection efficiency for more penetrating third-harmonic radiation. The measured attenuation coefficient for zero thickness is given by expressing equation (6) as the ray-sum and using a Taylor expansion to give

$$\mu_0 = \frac{\mu_1 + f\mu_3}{1+f} \tag{7}$$

and the measured ray-sum is

$$-\ln(I_t/I_o) = \mu_1 t + \ln(1+f) - \ln[1 + f\exp(+\Delta\mu t)], \tag{8}$$

where $\Delta\mu = (\mu_1 - \mu_3)$, and the mono-energetic ray-sum is calculated as $\mu_0 t$.

2.4. Measurement of dose rate in air

Dosimetry measurements used an FMB IC plus ionization chamber (FMB Osney Mead, Oxford, UK, special order part number AHQ2371 M) and Keithley model 6487 picoammeter to monitor the incident primary beam. The active chamber volume is 140 mm × 15 mm × 50 mm (beam width by height, times length along the beamline), with 18 mm electrode gap, 30 µm-thick kapton windows with area 145 mm × 18 mm, and recommended bias of up to +1.7 kV. This instrument measures the product of dose rate in air and beam area. But as the IMBL chamber and ammeter combination are not calibrated to do this, the instantaneous chamber current is reported instead. The beam had to be collimated to a smaller area which was estimated from images captured by the QUARTZ image receptor. Measurements were conducted at the rocking curve peak, at dose rates of 10–100 mGy s^{-1}, for principal beam energies in the range 25–100 keV. For this regime, the influence of recombination losses and electron migration losses are small (Crosbie *et al.*, 2013) and we assume their correction factors are unity. In the following, absorbed dose in air is described by the quantity air kerma (kinetic energy released per unit mass of absorber).

The relationship between ion chamber current I and air kerma rate is given by Bragg–Gray cavity theory (see, for example, Greening, 1981) as

$$\frac{\mathrm{d}K_{\mathrm{air}}}{\mathrm{d}t} = \frac{I}{m}\left(\frac{\overline{W}_{\mathrm{air}}}{e}\right), \tag{9}$$

where m is the mass of air in the irradiated volume and $(\overline{W}_{\mathrm{air}}/e)$ equals 33.97 J C^{-1} for air. The mass of air is estimated as the product of collimated beam area measured using an image receptor, 50 mm chamber length, and the density of air. We assumed dry air at normal temperature and pressure (density 1.204 kg m^{-3}) and a unity correction factor for temperature, pressure and humidity. For the beam collimated to 100 mm × 10 mm, the mass of irradiated air is 60.2 mg and chamber calibration used the ratio of air kerma to measured chamber current 0.564 mGy s^{-1} nA^{-1}.

The CTDI in air was measured in axial mode for the beam collimated to 10 mm thickness, using an Unfors Xi radiation measurement system (Unfors RaySafe AB, Billdal, Sweden). The CT probe is an air-filled ionization chamber with cylindrical geometry (7.5 mm outer diameter, 12.5 mm-thick sleeve and 100 mm active probe length). The specifications state that it is calibrated for medical CT beams (80–150 kVp tungsten radiation) with RQA, RQR and RQT beam qualities, responds to dose rates of 20 µGy s^{-1} to 100 mGy s^{-1}, and that the uncertainty is 5%. These beam qualities (IEC, 2012) translate to half-value layers of 7–13 mm aluminium at 80–150 kVp. The measurements were repeated ten months apart after an upgrade to the cooling system for the DCBLM.

2.5. Absorbed dose in phantoms during CT scans

The Unfors was also used to measure CTDI within cylindrical PMMA phantoms (see Fig. 3) of 140 mm length with diameters of 35 mm (mouse body), 50 mm (small animal body), 100 mm (child head), 160 mm (adult head) and 320 mm (adult body). The adult head and adult body phantoms were commercially available test objects (manufacturers include CIRS Inc, Leeds Test Objects, West Physics and others), while the remainder were custom-built for this project. The phantoms were scanned over the course of a CT scan with the probe positioned in one hole while all others were sealed with PMMA plugs (with the exception of the mouse body phantom that only features one central aperture). CT scans were performed over 360° with rotation times of approximately 20 s. The measurement process was triggered by the Unfors microprocessor identifying when the dose rate crosses a factory-set threshold. A series of test runs identified this threshold to be near 15 µGy s^{-1}, which motivated performing the experiments with maximum dose rates available at the rocking curve peak. Measurements were repeated for chamber positions at the central axis and along the periphery at 12 o'clock (pointing towards the source), 3, 6 and 9 o'clock positions. Where possible, the measurements considered beam energies of 25–100 keV. The thicker samples could not be measured at the lowest energy. The 320 mm adult body phantom (14.5 kg) proved to be too heavy for the rotation stage motor, while the second heaviest 160 mm-diameter adult head phantom of 3.6 kg was within the load tolerances of the stage.

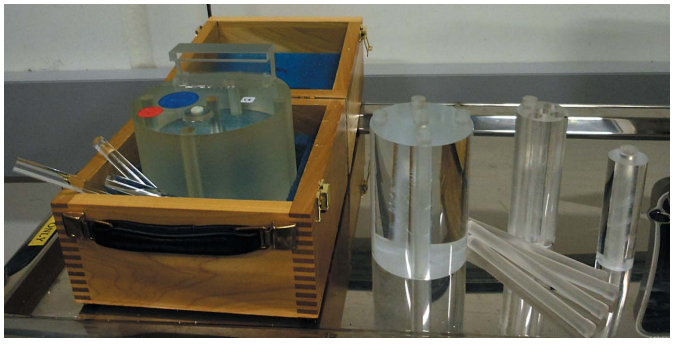

Figure 3
CT dosimetry phantoms representing (left to right): adult head (diameter 160 mm), paediatric head (100 mm), small animal (50 mm) and mouse (35 mm). Holes in the centre and positioned around the periphery at 3, 6, 9 and 12 o'clock (towards the source) receive the CT ion chamber (not shown) or removable 12 mm-diameter by 14 cm-long PMMA inserts.

3. Results

In early 2016 and prior to the DCBLM cooling system upgrade, we conducted beam quality measurements at 30–60 keV using the QUARTZ image receptor. The results (not presented) found a near linear relationship between measured ray-sums and thickness, suggesting less than 0.5% contribution from third-harmonic radiation at 30 keV and higher energies. In late 2016, the QUARTZ image quality was found to be degraded by structured artefacts and increased dark signal. Whilst localized areas of opacity could be suppressed by the flat-field correction, dark signal mean pixel values had increased from 160 ± 20 to 1100, and the noise-to-signal ratio for corrected images representing transmittance increased from 1% to 4%.

Figs. 4 and 5 present transmission measurement results for the QUARTZ image receptor (February 2016) and RUBY image receptor (December 2016), respectively. These are shown in Figs. 4(*a*) and 5(*a*) as the measured ray-sum via equation (5) as a function of copper thickness, with a straight line to denote contribution from the principal component alone based upon equation (6) and the NIST tabulation (Hubbell & Seltzer, 1995). In Figs. 4(*b*) and 5(*b*), results are depicted as the expected mono-energetic ray-sum as a function of measured ray-sum. The results for QUARTZ are anomalous, as the beam appears to become less penetrating or 'softer' for greater thicknesses of copper. In order to facilitate the quantitative interpretation of other measurements obtained with this detector, the non-linear response shown in Fig. 4(*b*) was re-expressed as the mono-energetic and measured transmittance and fitted to a quadratic.

The measurements with the RUBY image receptor shown in Fig. 5 used a suitable thickness of copper to provide more data points in the vicinity of ray-sums close to 5, where third-harmonic radiation is of some significance. Fitting against equation (5) with *Gnuplot* (see, for example, Williams & Kelley, 2011; Janert, 2016) and using the NIST attenuation coefficients summarized in Table 4, the third-harmonic contributions f were 2.65% (25 keV), 0.4% (30 keV and

Table 4
Linear attenuation coefficients (Hubbell & Seltzer, 1995) for copper (density 8.96 g cm^{-3}) and radiation path lengths $l = 1/\mu$.

Principal energy			Third harmonic		
E (keV)	μ (cm^{-1})	l (mm)	E (keV)	μ (cm^{-1})	l (mm)
25	162.3	0.062	75	7.975	1.254
30	97.32	0.103	90	5.158	1.939
35	63.10	0.158	105	3.694	2.707
40	43.37	0.231	120	2.850	3.509
45	31.20	0.321	135	2.335	4.283
50	23.31	0.429	150	1.977	5.058
60	14.20	0.704	180	1.567	6.382
80	6.806	1.469	240	1.182	8.460
100	4.089	2.446	300	0.998	10.020

35 keV) and 0.6% (40 keV). *Gnuplot* does not provide Pearsons correlation coefficients for linear models or rank correlation coefficients (such as Spearmans and Kendalls) for non-linear models. Instead, the goodness of fit is presented as the uncertainty for parameter f, which is 3.3% (25 keV) and

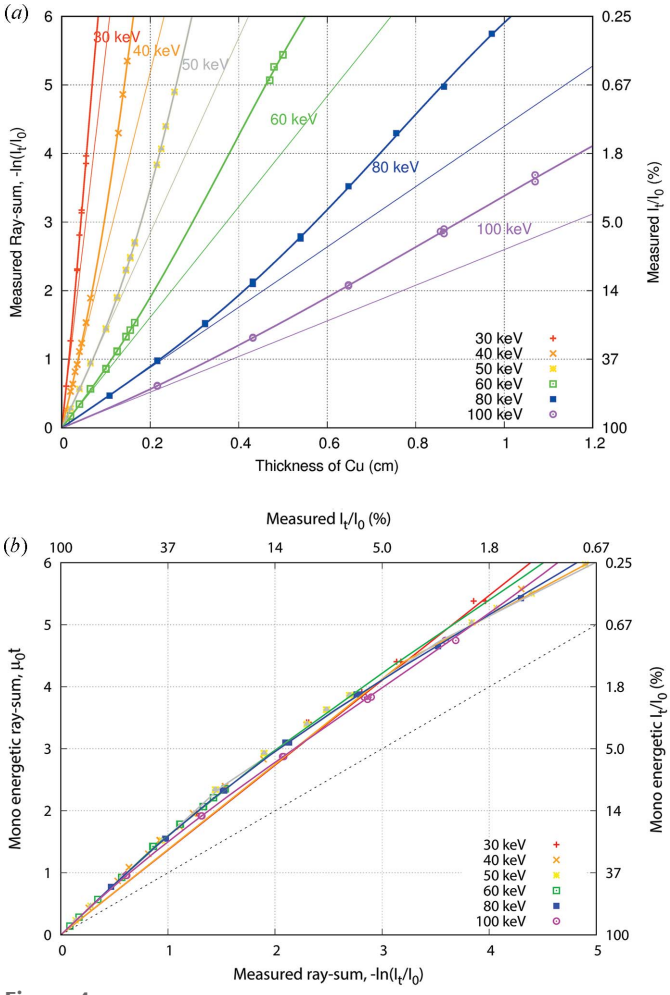

Figure 4
Transmission measurements (points) for copper using the QUARTZ image receptor and fitted curves based on equation (5). (*a*) Measured ray-sums $-\ln(I_t/I_o)$ against thickness, and (*b*) mono-energetic ray-sums $\mu_0 t$ via equation (6) against measured ray-sums, also showing (grey line) the ideal relationship.

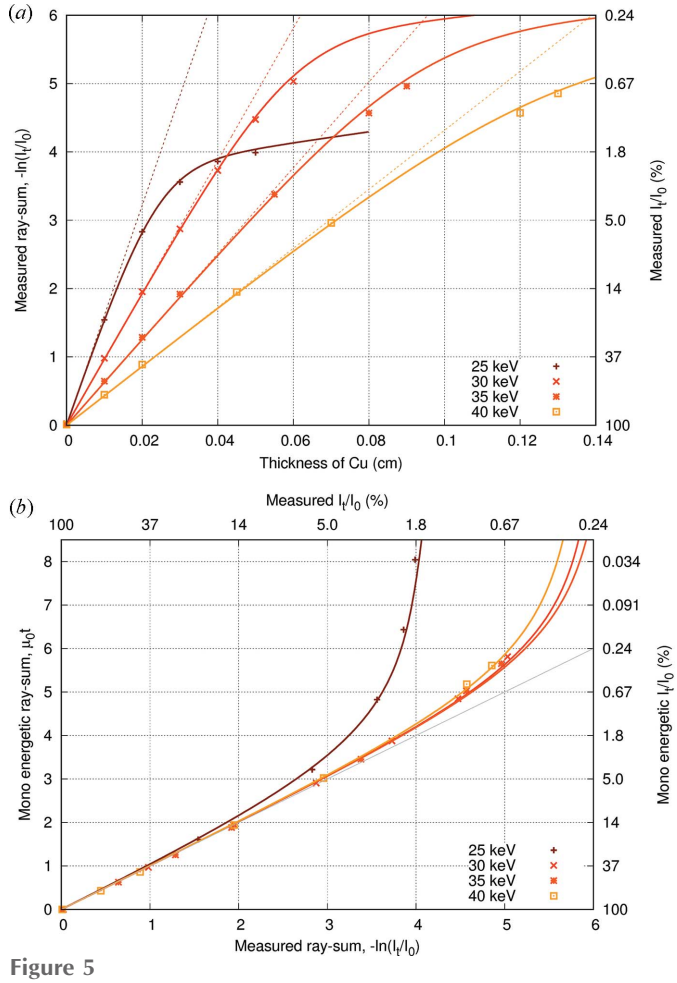

Figure 5
Transmission measurements (points) for copper using the RUBY image receptor and fitted curves based on equation (5). (*a*) Measured ray-sums $-\ln(I_t/I_o)$ against thickness, and (*b*) mono-energetic ray-sums $\mu_0 t$ via equation (6) against measured ray-sums, also showing (grey line) the ideal relationship.

17–24% (other energies), and the weighted sum of the root mean square of residuals, which is 2.2×10^{-5} (25 keV) and 5.2×10^{-5} to 15.2×10^{-5} (30–40 keV).

Air kerma rates are presented in Fig. 6 for set beam energies in the range 25–100 keV. The measurements with the FMB ion chamber were compromised by misalignment of the device whereby the primary beam struck the chamber walls. This led to an approximately fivefold increase in the amount of ionization collected, so these results are presented in relative units. The right-hand side of Fig. 6 shows air kerma rates for medical CT scanners (IMPACT, 1998) operated with 80–140 kVp. X-ray tube currents are typically hundreds of milliamps for the short duration of the scan, 0.3–2 s, subject to a power limit at higher kVp and a current limit for low kVp imposed by space charge effects (see, for example, Bushberg *et al.*, 2012; Flower, 2012).

The CTDI measurements in phantoms are normalized to the CTDI measured in air and are presented in Figs. 7 and 8. Two sets of measurements are presented because, during the first attempt, the Unfors dosimeter developed a fault involving the temperature and pressure sensor chip, leading to system

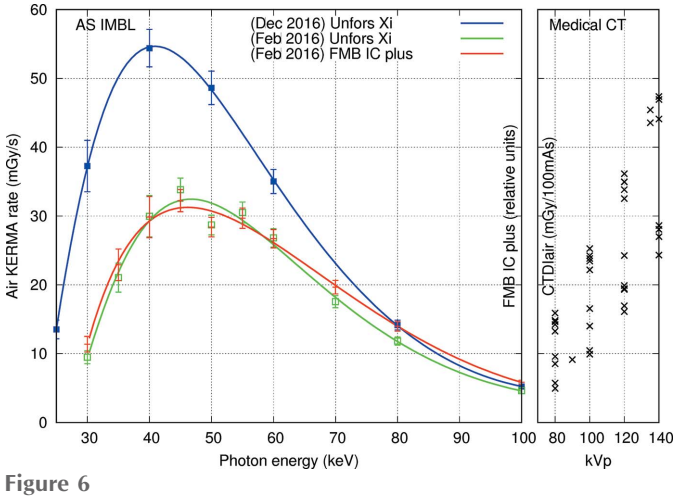

Figure 6
Air kerma rates measured at the rocking curve peak for the AS IMBL (left) and published (right) (IMPACT, 1998) CTDI in air for modern medical CT scanners, normalized to 100 mA tube current.

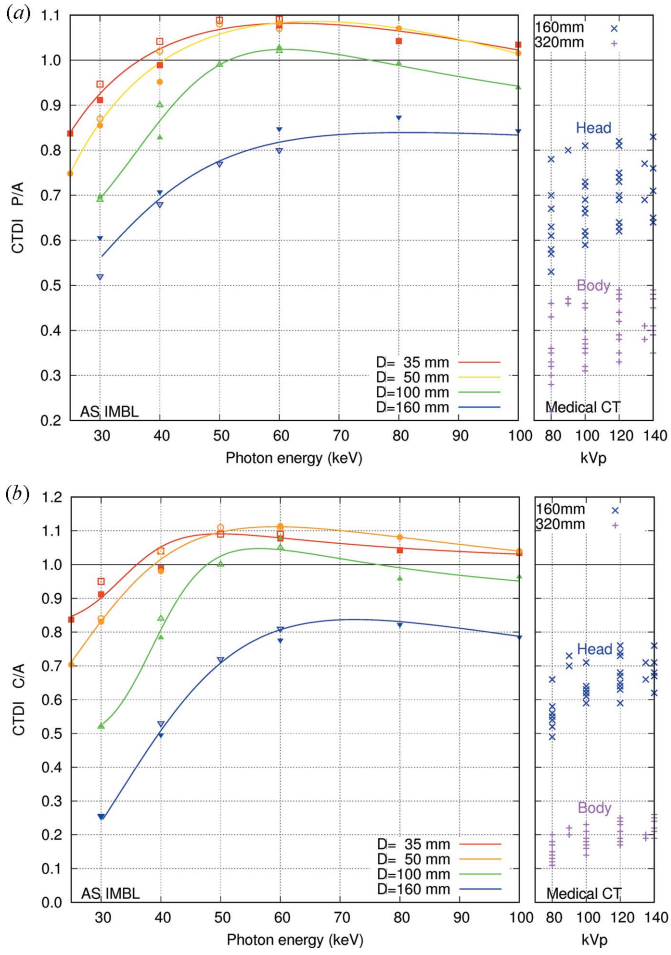

Figure 7
CTDI ratios for the AS IMBL using open (February 2016) and closed (December 2016) points, versus medical CT: (*a*) peripheral to air kerma and (*b*) central to air kerma.

shutdown. The peripheral value is the mean for the measurements at positions 3, 6, 9 and 12 o'clock. Fig. 8 shows the ratio of central to peripheral CTDI and the ratio of

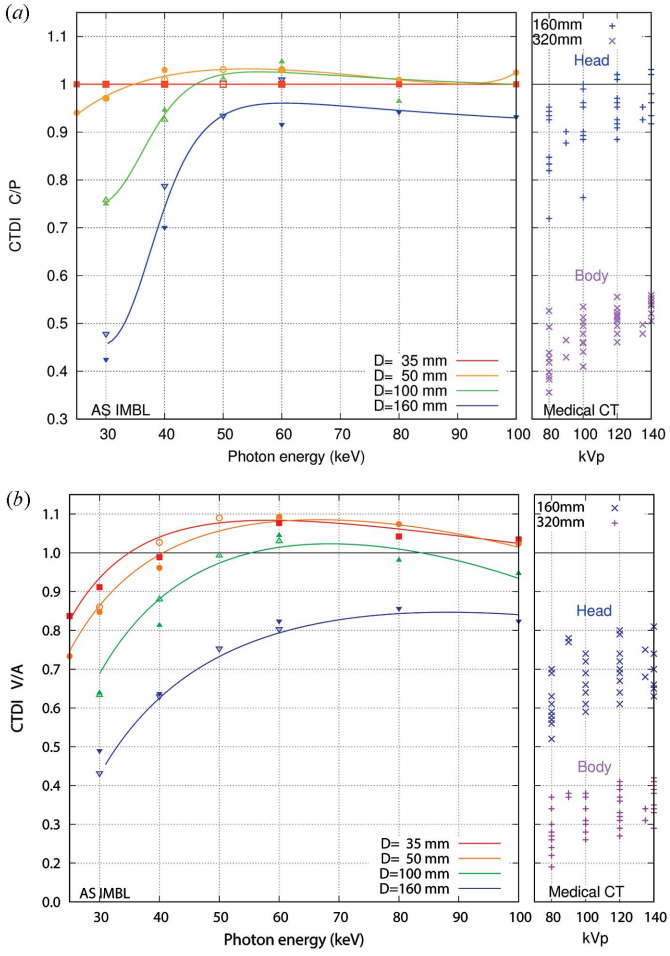

Figure 8
CTDI ratios for the AS IMBL using open (February 2016) and closed (December 2016) points, versus medical CT: (*a*) centre to peripheral and (*b*) volumetric to air kerma.

volumetric CTDI to CTDI in air. Also shown are values for modern medical CT scanners.

4. Discussion

Harmonic radiation introduces non-linearity to the relationship between measured ray-sum and thickness in equation (8), leading to systematic errors in the CT reconstruction known as beam hardening artefacts. For a homogeneous object, these manifest as reduced attenuation coefficients at the centre compared with the edge (cupping artefact), while strongly attenuating features produce streaks in preferred directions to obscure nearby structures.

The ideal instrument for characterizing harmonic content has a wide dynamic range, such as an ion chamber (Tran *et al.*, 2003; Barnea *et al.*, 2011), enabling measurements after strong attenuation (ray-sums of 10 or more) where the beam is dominated by harmonic radiation. Instead, we used the available image receptors, which respond to rays-sums up to about 5 (or 0.7% transmission), beyond which measurements are dominated by additive noise sources from the dark signal and afterglow for CsI-based systems. Within this limited range,

measurements span a linear region dominated by the principal component, to a shoulder region where the influence of harmonic radiation is small. Step wedges were designed with six thicknesses of copper sampling rays-sums to 5, and the design considerations for each beam energy are summarized in Table 3. The results in Fig. 5 show the harmonic contribution to be 2.7% at 25 keV and less than 0.5% at 30 keV and higher. Measurements at 20 keV (not presented) found harmonic radiation alone. These investigations also identified non-linearities (Fig. 4) in the response of the QUARTZ image receptor. It is likely that the QUARTZ image receptor has undergone radiation damage, producing opacities in the CsI, while changes to the front-end electronics have led to increased dark signal and non-linear response.

The incident air kerma rate controls the radiation absorbed dose to the sample, and the noise in the CT reconstruction. The measured air kerma rate has peak intensity near 40 keV with the full width at half maximum extending from 28 keV to 66 keV. The mean energy near 55 keV is twice that for SCMPW radiation despite Bragg diffraction being more efficient for lower energies. Lower-energy photons are preferentially removed by the filter materials in Hutch 1A and transmission through the DCBLM silicon crystals, whilst the air kerma dose payload is weighted by energy. Our measurements (Fig. 6) found increased output as improved cooling reduced the amount of lattice distortion in the DCBLM. The comparison against radiation output for white-beam medical CT shows the IMBL is now capable of delivering similar air kerma rates. The key differences are that the IMBL delivers a beam that is near mono-energetic and is operated continuously.

The ratio of CTDI measured in the phantom to CTDI in air (Figs. 7 and 8) can exceed unity due to backscattering, especially for smaller samples, whilst for larger specimens attenuation reduces this ratio. The peripheral CTDI measurements found that the 12 o'clock position, oriented towards the source, received 2% more radiation, a consequence of rotation stage inertia leading to a slow start for each scan. This can be avoided by introducing a delay of approximately 0.5 s between the start of sample rotation and opening the beam shutter. Medical CT makes use of bow-tie filters to attenuate the edges of the beam, so that the transmitted intensity profile is near uniform. This strategy makes best use of the available image receptor dynamic range, whilst also reducing the absorbed dose at the edges of the sample, which translates to reduced dose to organs at shallow depth. Synchrotron CT systems are yet to accommodate bow-tie filters tailored to the sample size. Fig. 8(*a*) shows the ratio of central to peripheral CTDI. The ratio is near unity for paediatric CT (not shown) and adult head CT, and approximately 0.5 for adult body CT. For IMBL CT the ratio is less than unity for thicker samples and lower energies reaching unity for energies above 50 keV and for small sample diameters of 35–50 mm. The introduction of bow-tie filters for synchrotron CT would be expected to decrease peripheral CTDI especially for thicker samples and photon energies below 50 keV.

The ratios of CTDIvol to CTDIair presented in Fig. 8(*b*) can be used to scale the cumulative air kerma recorded by an in-beam probe (*e.g.* an ion chamber that is larger than the incident beam) to estimate the average absorbed dose per unit length. These ratios exceed values currently achieved by medical CT scanners due the absence of a beam-shaping bow-tie filter. The dose length product (DLP) is a measure of the average absorbed dose to the scanned volume, and is given by the product of CTDIvol and scanned axial length divided by the helical pitch, which is unity for contiguous axial segments.

CT dose calculators are available to estimate organ dose and the effective dose for medical CT scanners using axial and helical scan protocols. Results were summarized in Fig. 2(*a*) for different body regions, beam qualities and patient age groups. Small-animal dosimetry for laboratory micro-CT systems with white radiation has been measured experimentally using thermoluminescent dosimeters (TLD) placed on the surface (Goertzen *et al.*, 2002) and by Monte Carlo methods (Boone *et al.*, 2004). Further work is required to extend these models and calculations to synchrotron CT with near mono-energetic radiation and for appropriate beam-shaping (bow-tie) filters for research involving CT scans of laboratory animals.

5. Conclusions

The measured beam intensities, expressed as incident air kerma rate at the axis of rotation in Fig. 6, show that the AS IMBL DCBLM now delivers mono-energetic radiation at air kerma rates comparable with white-beam medical CT. Dosimetry measurements with phantoms identified that inertia slows the rotation speed at the start and end at start of each CT scan, and the Unfors Xi trigger threshold for CTDI measurements is 15 μGy s^{-1}.

Beam quality investigations using the IMBL image receptors to measure transmission through suitable thicknesses of copper (Table 3) found that their dynamic range is limited by the dark signal to a maximum ray-sum near 5, or 0.7% transmission. The QUARTZ image receptor was found to exhibit a non-linear response at all energies (Fig. 4), which can be characterized using a quadratic relationship to rescale measured to mono-energetic ray-sums. Measurements with the RUBY image receptor found that the fractional contribution from third-harmonic radiation is insignificant at energies above 35 keV, 0.5% at 30 keV, 2.7% at 25 keV and near 100% at lower energies.

An estimate of the absorbed dose delivered during CT can be gained with the following approach. The amount of incident radiation is monitored using a wide area detector such as an ion chamber to record the product of air kerma rate and beam area, and their integral over the duration of the CT scan. With knowledge of the collimated beam area and exposure time, these can be scaled to estimate the air kerma at the isocentre. The results presented in Fig. 8(*b*) scale CTDI in air to CTDIvol according to beam energy and sample diameter. The DLP for the volume scan is the product of CTDIvol and scan length and can be used by the medical CT dose calcula-

tors to estimate organ doses and effective dose for human imaging.

CT dose calculators for small-animal imaging are yet to be developed, and appropriate tissue weighting factors are not available for estimating effective dose. Until this is resolved, the results in Fig. 8 can be used to estimate absorbed dose to individual organs for animals exposed to the primary beam. The introduction of bow-tie filters for synchrotron CT would be expected to improve image quality and reduce the absorbed dose to the surface and organs at shallow depth, and would require new measurements of the CTDI ratios presented in Figs. 7 and 8.

Acknowledgements

This research was undertaken on the Imaging and Medical Beamline at the Australian Synchrotron, part of ANSTO, experiment numbers AS 8795 (February 2015), AS 9365 (August 2015), EU 10886 and AS 10268 (24–25 February 2016) and AS 11143 (10–12 December 2016). We thank South Australia Medical Imaging (SAMI) and Barwon Health for the loan of their Unfors dosimetry systems, and Alfred Health for the loan of their CTDI adult head and body phantoms.

Funding information

NS gratefully acknowledges funding from a University of Otago Research Grant 2016. SM and NS acknowledge travel funding provided by the International Synchrotron Access Program (ISAP) managed by the Australian Synchrotron, part of ANSTO, and by the New Zealand Synchrotron Group, and funded by the Australian and New Zealand Governments, respectively.

References

ARPANSA (2005). *Code of practice for the exposure of humans to ionising radiation for research purposes.* Report RPS8. Australian Radiation Protection and Nuclear Science Agency, Miranda, New South Wales, Australia.

ARPANSA (2011). *Australian national diagnostic reference levels for MDCT – Adult.* Report. Australian Radiation Protection and Nuclear Science Agency, Miranda, New South Wales, Australia.

ARPANSA (2012). *Australian national diagnostic reference levels for MDCT – Paediatric.* Report. Australian Radiation Protection and Nuclear Science Agency, Miranda, New South Wales, Australia.

Attwood, D. (2000). *Soft X-rays and Extreme Ultraviolet Radiation.* Cambridge University Press.

Barnea, Z., Chantler, C. T., Glover, J. L., Grigg, M. W., Islam, M. T., de Jonge, M. D., Rae, N. A. & Tran, C. Q. (2011). *J. Appl. Cryst.* **44**, 281–286.

Boone, J., Velazquez, O. & Cherry, S. R. (2004). *Mol. Imaging*, **3**, 149–158.

Bravin, A., Coan, P. & Suortti, P. (2013). *Phys. Med. Biol.* **58**, R1–35.

Bushberg, J. T., Seibert, J. A., Leidholdt, E. M., & Boone, J. M. (2012). *The Essential Physics of Medical Imaging*, 3rd ed. Philadelphia: Lippincott Williams and Wilkins.

Carmi, R., Naveh, G. & Altman, A. (2005). *IEEE Nucl. Sci. Symp. Conf. Rec.* **4**, 1876–1878.

Chapman, D., Thomlinson, W., Johnston, R. E., Washburn, D., Pisano, E., Gmür, N., Zhong, Z., Menk, R., Arfelli, F. & Sayers, D. (1997). *Phys. Med. Biol.* **42**, 2015–2025.

Cristy, M. & Eckerman, K. (1987). *Specific Absorbed Fractions of Energy at Various Ages from Internal Photon Sources. I. Methods.* Report ORNL/TM-8381/V1. Oak Ridge National Laboratory, TN, USA.

Crosbie, J., Rogers, P. A. W., Stevenson, A. W., Hall, C. J., Lye, J. E., Nordström, T., Midgley, S. M. & Lewis, R. A. (2013). *Med. Phys.* **40**, 062103–1.

Deak, P., Smal, Y. & Kalender, W. A. (2010). *Radiology*, **257**, 158–166.

Eijk, C. W. van (2002). *Phys. Med. Biol.* **47**, R85–R106.

Flohr, T., McCollough, C. H., Bruder, H., Petersilka, M., Gruber, K., Süß, C., Grasruck, M., Stierstorfer, K., Krauss, B., Raupach, R., Primak, A. N., Küttner, A., Achenbach, S., Becker, C., Kopp, A. & Ohnesorge, B. M. (2006). *Eur. Radiol.* **16**, 256–268.

Flower, M. (2012). *Webb's Physics of Medical Imaging*, 2nd ed. Boca Raton: CRC Press.

Freneau, A., Dos Santos, M., Voisin, P., Tang, N., Bueno Vizcarra, M., Villagrasa, C., Roy, L., Vaurijoux, A. & Gruel, G. (2018). *Int. J. Radiat. Biol.* **94**, 1075–1084.

Goertzen, A., Meadors, A. K., Silverman, R. W. & Cherry, S. R. (2002). *Phys. Med. Biol.* **47**, 4315–4328.

Greening, J. (1981). *Fundamentals of Radiation Dosimetry.* Bristol: Hilger.

Hall, C., Hausermann, D., Maksimenko, A., Astolfo, A., Siu, K., Pearson, J. & Stevenson, A. (2013). *J. Instrum.* **8**, C06011.

Hubbell, J. & Seltzer, S. (1995). *Tables of X-ray Mass Attenuation Coefficients 1 keV to 20 MeV for Elements Z = 1 to 92 and 48 additional substances of dosimetric interest.* Report NISTIR 5632. National Institute of Standards and Technology, Gaithersburg, MD, USA.

ICRP (2007). *The 2007 Recommendations of the International Commission on Radiological Protection.* Technical Report. ICRP Publication 103. International Commission on Radiological Protection.

ICRP (2011). *Statement of tissue reactions (21 April 2011).* Statement ICRP ref 4825-3093-1464. International Commission on Radiological Protection.

ICRP (2012). *Statement on tissue reactions and early and late effects of radiation in normal tissues and organs threshold doses for tissue reactions in a radiation protection context (February 2012).* Technical Report. Annals of the ICRP 41 (1–2). International Commission on Radiological Protection.

IEC (2012). *Medical electrical equipment – Dosimeters with ionization chambers and/or semiconductor detectors as used in X-ray diagnostic imaging.* Technical Report IEC 61674. International Electrotechnical Commission.

IMPACT (1998). *IMPACT CT Scanner Evaluation Reports (1998–2010).* http://www.impactscan.org/bluecover.htm. Imaging Performance Assessment of CT Scanners. Imaging Physics Section of the Medical Physics Department at St George's Hospital, Tooting, London, UK.

IMPACT (2011). *IMPACT CT Dosimetry Tool; CTDI calculator*, Version 1.0.4. Excel spreadsheet. Imaging Performance Assessment of CT Scanners. Imaging Physics Section of the Medical Physics Department at St George's Hospital, Tooting, London, UK.

Jackson, D. & Hawkes, D. (1981). *Phys. Rep.* **70**, 169–233.

Janert, P. (2016). *Gnuplot in Action: Understanding Data with Graphs.* Greenwich: Manning Publications.

Li, B., Yadava, G. & Hsieh, J. (2011). *Med. Phys.* **38**, 2595–2601.

Liaparinos, P., Kandarakis, I. S., Cavouras, D. A., Delis, H. B. & Panayiotakis, G. S. (2006). *Med. Phys.* **33**, 4502–4514.

Mahesh, M. (2009). *MDCT Physics: The Basics – Technology, Image Quality and Radiation Dose.* Philadelphia: Lippincott Williams and Wilkins.

Midgley, S. (2006). *Rad. Phys. Chem.* **75**, 836–944.

Midgley, S. & Schleich, N. (2015). *J. Synchrotron Rad.* **22**, 807–818.

NHMRC (2013). *Australian Code of Practice for the Care and Use of Animals for Scientific Purposes*, 7th edition. National Health and Medical Research Council, Canberra, Australia.

Nikjoo, H. & Lindborg, L. (2010). *Phys. Med. Biol.* **55**, R65–109.
Nördfors, B. (1960). *Arkiv. Fys.* **18**, 37–47.
NRC (2006). *Health Risks from Exposure to Low Levels of Ionizing Radiation.* Report BEIR VII – Phase 2. National Research Council, Washington, DC, USA.
Petersilka, M., Bruder, H., Krauss, B., Stierstorfer, K. & Flohr, T. G. (2008). *Eur. J. Radiol.* **68**, 362–368.
Rose, R. & Shapiro, M. (1948). *Phys. Rev.* **74**, 1853–1864.
Schlomka, J., Roessl, E., Dorscheid, R., Dill, S., Martens, G., Istel, T., Bäumer, C., Herrmann, C., Steadman, R., Zeitler, G., Livne, A. & Proksa, R. (2008). *Phys. Med. Biol.* **53**, 4031–4047.
Schneider, C., Rasband, W. S. & Eliceiri, K. W. (2012). *Nat. Methods*, **9**, 671–675.
Stamm, G. & Nagel, H. (2002). *ROFO Fortschr. Geb. Rontgenstr. Nuklearmed.* **174**, 1570–1576.
Stevenson, A. W. (2017). *Biomed. Phys. Eng. Express*, **4**, 015009.
Stevenson, A. W., Crosbie, J. C., Hall, C. J., Häusermann, D., Livingstone, J. & Lye, J. E. (2017). *J. Synchrotron Rad.* **24**, 110–141.
Stevenson, A. W. & Di Lillo, F. (2017). *J. Synchrotron Rad.* **24**, 939–953.
Stevenson, A. W., Hall, C. J., Mayo, S. C., Häusermann, D., Maksimenko, A., Gureyev, T. E., Nesterets, Y. I., Wilkins, S. W. & Lewis, R. A. (2012). *J. Synchrotron Rad.* **19**, 728–750.
Tran, C., Barnea, Z., de Jonge, M. D., Dhal, B. B., Paterson, D., Cookson, D. J. & Chantler, C. T. (2003). *X-ray Spectrom.* **32**, 69–74.
Webb, S. (1990). *From the Watching of Shadows: the Origins of Radiological Tomography.* Boca Raton: CRC Press.
Wilkins, S., Gureyev, T. E., Gao, D., Pogany, A. & Stevenson, A. W. (1996). *Nature*, **384**, 335–338.
Williams, T. & Kelley, C. (2011). *Gnuplot 5.2: an interactive plotting program*, Version 5.2, http://www.gnuplot.info.